

1 *Research article*

2

3 ***Txn1* mutation causes epilepsy associated with vacuolar degeneration in the**
4 **midbrain**

5 Iori Ohmori^{*1,2}, Mamoru Ouchida³, Hirohiko Imai⁴, Saeko Ishida⁵, Shinya Toyokuni⁶, Tomoji
6 Mashimo⁵.

7

8 ¹ Section of Developmental Physiology and Pathology, Education, Institute of Academic and
9 Research, Okayama University, Tsushima 3-chome 1-1, Kita-ku, Okayama 700-8530, Japan

10 ² Department of Child Neurology, Medicine, Dentistry and Pharmaceutical Sciences,
11 Okayama University, Shikatacho 2-chome 5-1, Kita-Ku, Okayama 700-8558, Japan.

12 ³ Department of Molecular Oncology, Medicine, Dentistry and Pharmaceutical Sciences,
13 Institute of Academic and Research, Okayama University, Shikatacho 2-Chome 5-1, Kita-Ku,
14 Okayama 700-8558, Japan.

15 ⁴ Department of Systems Science, Kyoto University Graduate School of Informatics,
16 Yoshida-Honmachi, Sakyo-ward, Kyoto 606-8501, Japan.

17 ⁵ Division of Animal Genetics, Laboratory Animal Research Center, Institute of Medical
18 Science, The University of Tokyo, Tokyo, 108-8639, Japan.

19 ⁶ Department of Pathology and Biological Responses, Nagoya University Graduate School of
20 Medicine, 65 Tsurumai-Cho, Showa-Ku, Nagoya 466-8550, Japan

21

22

23

24 ***Correspondence:** iori@md.okayama-u.ac.jp

25

26

28 **Abstract**

29 Thioredoxin (TXN), encoded by *Txn1*, acts as a critical antioxidant in the defense against
30 oxidative stress by regulating the dithiol/disulfide balance of interacting proteins. The role of
31 TXN in the central nervous system (CNS) is largely unknown. A phenotype-driven study of
32 *N*-ethyl-*N*-nitrosourea-mutated rats with running seizures at around five-week of age revealed
33 the relevance of *Txn1* mutations to CNS disorders. Genetic mapping identified *Txn1*-F54L in
34 epileptic rats. The insulin-reducing activity of *Txn1*-F54L rats was approximately one-third
35 that of the wild-type. Vacuolar degeneration in the midbrain, mainly in the thalamus and the
36 inferior colliculus, was observed in the *Txn1*-F54L rats. The lesions displayed neuronal and
37 oligodendrocyte cell death. Neurons in *Txn1*-F54L rats showed morphological changes in the
38 mitochondria. Vacuolar degeneration began at three weeks of age, and spontaneous repair
39 began at seven weeks; a dramatic change from cell death to repair occurred in the midbrain
40 during a restricted period. In conclusion, *Txn1* is essential for the development of the
41 midbrain in juvenile rats.

42

43 **Keywords**

44 *Txn1*, Thioredoxin, mitochondria, neuron, vacuolar degeneration, epilepsy, oxidative stress

45

46 **List of abbreviations**

47 CNS, central nervous system;

48 WT, wild type;

49 ROS, reactive oxygen species

50 NADPH, Nicotinamide adenine dinucleotide phosphate;

51 NOX, NADPH oxidases;

52 ENU, N-ethyl-N-nitrosourea

53 SOD, superoxide dismutase;

54 CAT, catalase;

55 HD, Huntington's disease;

56 ALS, amyotrophic lateral sclerosis;

57 MS, multiple sclerosis;

58 GSH, Glutathione;

59 GPx, glutathione peroxidase;

60 Prdx, peroxiredoxin

61 Txn, thioredoxin;

62 MRI, magnetic resonance imaging;

63 8-OHdG, 8-hydroxy-2'-deoxyguanosine;

64 4-HNE, 4-hydroxynonenal

65 TUNEL, Terminal deoxynucleotidyl transferase-mediated dUTP Nick End Labeling

66 PBS, phosphate-buffered saline;

67 HE, hematoxylin and eosin;

68 KB, Klüber-Barrera

69 DAB, 3,3'-diaminobenzidine;

70 IHC, immunohistochemistry;

71 GFAP, glial fibrillary acidic protein;

72 GAPDH, Glyceraldehyde 3-phosphate dehydrogenase

73 TEM, Transmission electron microscope;

74

75 **Introduction**

76 The brain is more vulnerable to oxidative stress than other organs. Compared to the liver or
77 kidney, the brain has a higher oxygen consumption, in some areas has an increased iron
78 content that catalyzes the generation of reactive oxygen species (ROS), has elevated amounts
79 of lipids with unsaturated fatty acids, and has lower activities of superoxide dismutase (SOD),
80 catalase (CAT), and glutathione peroxidase (GPx) [1]. Several studies have implicated
81 oxidative stress in the development of neurodegenerative diseases such as Alzheimer's
82 disease, Parkinson's disease, Huntington's disease (HD), amyotrophic lateral sclerosis (ALS),
83 and multiple sclerosis (MS) [2, 3, 4].

84

85 The primary endogenous sources of ROS in mammals are the mitochondrial respiratory chain
86 and NADPH oxidase (NOX). [5, 6, 7]. Oxidative stress modulates functions ranging from cell
87 homeostasis to cell death [8]. Low levels of mitochondrial ROS production under
88 physiological conditions are required for cellular signaling pathways, such as those regulating
89 proliferation and differentiation. In contrast, excess ROS causes protein denaturation and
90 promotes cell death. The delicate balance between the beneficial and harmful effects of ROS
91 is a vital aspect of living cells and tissues [8].

92

93 Living organisms have a defense system that scavenges ROS produced by mitochondria. The
94 enzymatic antioxidant system consists of SOD, CAT, GPx, and thioredoxin (Txn). Txn was
95 first identified as a hydrogen donor for ribonucleotide reductase in *Escherichia coli* [9]. In
96 humans, thioredoxin has been identified in the culture media of adult T-cell leukemia cell
97 lines and Epstein-Barr virus-infected cells [10]. Subsequently, it has been reported that
98 thioredoxin expression is upregulated in many cancer cells and that it inhibits apoptosis of
99 cancer cells [11, 12]. Accordingly, the thioredoxin system has attracted attention as a target

100 for cancer therapy [13, 14, 15]. However, fewer studies have investigated the roles of the
101 TXN system *in vivo*. A previous study reported that transgenic mice overexpressing a
102 dominant-negative mutant of *Txn1* specifically in the heart show cardiac hypertrophy [16].
103 Homozygous *Txn1* knockout mice are embryonically lethal, whereas heterozygous mice show
104 normal development [17]. Other than these reports, little is known about the effects of
105 reduced TXN activity *in vivo*.

106

107 Here, we present a novel animal model for neurodegeneration designated the
108 *Adem* “Age-dependent mitochondrial cytopathy” rat. These animals harbor a *Txn1* missense
109 mutation (F54L). *Adem* exhibit a unique seizure phenotype that appears only at 5 weeks of
110 age. Detailed histological analyses and anatomical analyses using MRI revealed vacuolar
111 degeneration in the midbrain during the epileptic period. Our study reveals a hitherto
112 unknown function of *Txn1* in the CNS.

113

114 **Materials and methods**

115 *Animals*

116 We used *Txn1*-F54L rats (*Adem*; Age-dependent mitochondrial cytopathy rat) generated by
117 ENU-mutagenesis and a *Txn1*- T160C (p. F54L) knock-in rat generated by CRISPR-Cas 9.
118 We used the former to characterize the phenotype and the latter to confirm the reproducibility
119 of the phenotype. The *Txn1*-F54L rat was initially discovered in an ENU-induced mutant
120 archive at Kyoto University [18, 19, <http://www.anim.med.kyoto-u.ac.jp/nbr>] as a rare strain
121 with frequent running seizures only in its juvenile stage. All animal husbandry procedures
122 were performed according to the protocols approved by the institutional experimental animal
123 use committees Okayama University, Osaka University, and Kyoto University. Both sexes
124 were used in the present study.

125

126 ***Genetic mapping and sequencing analysis of the Adem rat generated by ENU-mutagenesis***

127 The rats with running seizures were backcrossed for more than ten generations on the
128 *F344/NSlc* inbred background (Japan SLC, Hamamatsu, Japan). The repeated backcrosses
129 ensure that the frequency of potential mutations induced by ENU elsewhere in the genome is
130 reduced to approximately 1 in 4×10^6 bp of the genome. To identify the causative gene, we
131 produced 117 (*Adem* × *BN/SsNSlc*) × *BN/SsNSlc* backcross progeny. Genetic mapping of the
132 locus was determined in rats that displayed wild running or generalized tonic-clonic seizure
133 phenotypes. Genomic DNA was extracted from rat tail biopsies by an automatic genomic
134 DNA isolation system (PI-200; Kurabo, Osaka, Japan). To localize the locus to a specific
135 chromosomal region, genome-wide scanning on DNA samples was performed using simple
136 sequence length polymorphism (SSLP) markers covering all autosomal chromosomes (Chrs)
137 as previously reported [20].

138 To enrich the 1.5-Mb region (Chr 5: 75,159,000 to 76,708,000), SureSelect custom DNA
139 probes were designed by SureDesign under moderately stringent conditions, and generated by
140 Agilent Technologies (Santa Clara, CA, USA). The DNA library was prepared using
141 SureSelect reagents and a custom probe kit. Genomic sequence analysis was performed by
142 HiSeq 2500 (2×150 bp) according to the standard protocol at Takara Bio.

143

144 ***Generation of *Txn1*- T160C (p. F54L) knock-in rat using CRISPR-Cas 9***

145 The possibility of genomic DNA alterations around the *Txn1* gene could not be fully excluded
146 in *Txn1*-F54L rats generated by ENU mutagenesis. As the *Txn1* mutant rats showed a unique
147 phenotype, never previously reported, we generated a new *Txn1*-F54L knock-in rat to test the
148 reproducibility of this phenotype. A *Txn1* T160C (p. F54L) knock-in rat was generated by
149 CRISPR-Cas9 genome editing with long single-stranded DNA (lssDNA), as previously
150 reported [21]. A pair of guide RNAs (gRNAs) targeting intron 1 and intron 2 of rat *Txn1* were

151 designed. LssDNA for *Txn1* was synthesized using a long ssDNA Preparation Kit
152 (Biodynamics Laboratory Inc., Tokyo, Japan) following the manufacturer's protocol. The
153 sequences of gRNA and ssDNA are listed in Supplementary Table 1. Cas9 mRNA (400 ng/μl),
154 gRNA (200 ng/μl), and ssDNA (40 ng/μl) were delivered into 113 *F344/Jcl* embryos by
155 electroporation as previously reported [22]. The two-cell stage embryos (n = 110) were
156 transferred into the oviducts of five pseudopregnant females. Genomic DNA from founder
157 rats was extracted from the tail biopsies. The CRISPR target site was amplified using the
158 specific primer pairs listed in Supplementary Table 1.

159

160 ***Genotyping***

161 The last 3 mm of the rat tail was cut at three weeks of age, and DNA was purified with a
162 DNeasy Blood & Tissue kit (Qiagen, Hilden, Germany). A DNA fragment containing a
163 mutation was amplified with a pair of primers as follows: FW 5' - CCA CAT GGG AGA
164 GTC ACA T -3' and RV 5' - ATA GCC TGG AAG CGG TCA GAT G -3' (Sigma-Aldrich
165 Japan, Inc., Tokyo, Japan). The PCR products (521 bp) were then treated with the restriction
166 enzyme *Bsp1286I* (New England Biolabs, Ipswich, MA, USA), and the F54L mutant DNA
167 was digested to 260 bp and 261 bp fragments. Genotyping was determined by the size of the
168 digested fragments on a 3% agarose gel.

169

170 ***Video monitoring of epileptic seizures***

171 To clarify the appearance and frequency of epileptic seizures, both the heterozygotes (n = 8)
172 and homozygotes (n = 9) were placed under a 24-hour video monitoring system (Handycam
173 HDR-CX480, SONY, Japan) from week three to nine,

174

175 ***Histological analysis***

176 Brains were fixed with 10% formalin neutral buffer solution. Tissue sections were cut from
177 paraffin-embedded brain samples taken at 2, 3, 5, and 9 weeks of age and were subjected to
178 hematoxylin and eosin (HE) and Bodian and Klüver-Barrera (KB) staining using standard
179 protocols. The stained sections were examined under a BZX-700 microscope (Keyence,
180 Osaka, Japan). We evaluated brain lesions, including samples from the thalamus and the
181 inferior colliculus, in the sagittal and coronal planes.

182

183 *Head MRI*

184 To evaluate the extent of brain lesions and their changes over time, an MRI scan was
185 performed in 1 mm slices. Three animals were examined for each genotype at 5, 7, and 9
186 weeks of age. The same animal was examined twice on days 1 and 14 as the storage period of
187 the MRI-attached breeding room was limited to no longer than two weeks. The mice were
188 anesthetized with isoflurane and laid in the prone position on a cradle. Anesthesia was
189 maintained by inhalation of 2% isoflurane in air at 1.4 L/min through a face mask.
190 Throughout the MRI measurements, respiratory rate and rectal temperature were monitored
191 using a dedicated system (Model 1025, MR-compatible Small Animal Monitoring and Gating
192 System, SA Instruments, Inc., NY, USA). The body temperature was maintained by a flow of
193 warm air using a heater system (MR-compatible Small Animal Heating System, SA
194 Instruments).

195

196 All MR images were obtained with a 4.7 Tesla preclinical MR scanner (BioSpec 47/16 USR,
197 Bruker BioSpin MRI GmbH, Ettlingen, Germany). A quadrature volume resonator (Bruker
198 BioSpin) was used for signal detection. The scanner was operated using ParaVision 6.0.1
199 (Bruker BioSpin). Two-dimensional multi-slice T2-weighted MR imaging was performed
200 using a rapid acquisition with relaxation enhancement (RARE) sequence. The whole-head
201 images were acquired in three orthogonal (coronal, sagittal, and axial) orientations. The

202 acquisition parameters were as follows: echo time (TE), 12 ms; effective TE, 36 ms; RARE
203 factor, 8; acquisition bandwidth, 62.5 kHz; in-plane spatial resolution, $0.156 \times 0.156 \text{ mm}^2$;
204 slice thickness, 1 mm; slice gaps, 0 mm; the number of averages, 2. For coronal orientation,
205 repetition time (TR), 3000 ms; field of view (FOV), $25 \times 29.3 \text{ mm}^2$, matrix size, 120×136
206 (zero-filled to 160×188 before image reconstruction); the number of slices, 24; acquisition
207 time, 1 min 42 s. For sagittal orientation, TR, 2500 ms; FOV, $27 \times 27.5 \text{ mm}^2$, matrix size, 131
208 $\times 128$ (zero-filled to 173×176); number of slices, 18; acquisition time, 1 min 20 s. For axial
209 orientation, TR, 2500 ms; FOV, $27 \times 30.5 \text{ mm}^2$, matrix size, 131×144 (zero-filled to $173 \times$
210 195); the number of slices, 16; acquisition time, 1 min 30 s.

211

212 ***Western blotting***

213 Western blotting was used to quantify the different cell types of the brain lesion and Txn1
214 expression levels in multiple organs in the rats. The protein extracts (10 μg) from rat tissues
215 were mixed with sample buffer solution (Nakalai Tesque, Kyoto, Japan), denatured at $95 \text{ }^\circ\text{C}$
216 for 5 min, and loaded onto a sodium dodecyl sulfate (SDS)-polyacrylamide gel (Mini-protean
217 TGX Precast gels; Bio-Rad, Hercules, CA) for electrophoresis. The proteins were blotted onto
218 a polyvinylidene fluoride (PVDF) membrane using the iBlot Dry Blotting System (Thermo
219 Fisher Scientific). Membranes were incubated with anti-Thioredoxin1 rabbit antibody
220 (CST#2298; Cell Signaling Technology, Danvers, MA, USA), anti-NeuN rabbit antibody
221 (ab177487; Abcam, Cambridge, UK), anti-Olig2 rabbit antibody (ab109186; Abcam),
222 anti-glial fibrillary acidic protein (GFAP) rabbit antibody (ab7260; Abcam), anti-Iba1 rabbit
223 antibody (ab178847; Abcam), and anti-glyceraldehyde 3-phosphate dehydrogenase (GAPDH)
224 rabbit antibody (CST #2118). Mouse and rabbit primary antibodies were detected using
225 anti-mouse IgG-HRP-linked antibody (CST #7076) and anti-rabbit IgG-HRP-linked antibody
226 (CST; #7074), respectively. Chemiluminescence was detected using Western Lightning ECL
227 Pro (PerkinElmer Japan, Kanagawa, Japan) and the ChemiDoc Touch (Bio-Rad).

228

229 ***Immunohistochemistry (IHC) analyses***

230 A standard IHC protocol was used to stain the brain tissue samples. In brief, 5- μ m-sized
231 paraffin-embedded tissue sections were de-paraffinized with xylene. Antigen retrieval was
232 performed by autoclaving at 120 °C for 5 min. Endogenous peroxidases were quenched by
233 treatment with 0.3% hydrogen peroxide in methanol for 30 min at room temperature. They
234 were then incubated with blocking serum for 1 h at 22-26 °C. Sections were incubated with
235 the following primary antibodies to determine the cell type in the brain lesion: anti-NeuN
236 rabbit antibody (ab177487; Abcam, Cambridge, UK) and anti-Olig2 rabbit antibody
237 (ab109186; Abcam) for 1 h at room temperature. To determine DNA oxidative injury and
238 lipid peroxidation, sections were stained with anti-8-hydroxy-2'-deoxyguanosine (8-OHdG)
239 mouse antibody (MOG-020P, JaICA, Japan), and anti-4-hydroxynonenal (4-HNE) mouse
240 antibody (MHN-020P, JaICA, Japan) overnight at 4 °C, respectively. The sections were then
241 reacted with a biotinylated rabbit polyclonal secondary antibody (PK-6200, Vector
242 Laboratories, Burlingame, CA, USA). To reveal the staining, we used an avidin-biotinylated
243 peroxidase complex (PK-6200, Vector Laboratories). After washing, the slides were
244 incubated with 3,3'-diaminobenzidine (DAB) (SK-4100, Vector Laboratories) and
245 immediately washed with tap water after color development. The slides were then
246 counterstained with hematoxylin, mounted with dibutyl phthalate xylene (DPX) and observed
247 under a BZX-700 multifunctional microscope (Keyence, Osaka, Japan). Quantification of
248 IHC was performed by assessing five randomly selected fields in the inferior colliculus and
249 thalamus. The percentages of positive cells or positive areas were calculated using BZX
250 Analyzer software (Keyence).

251

252 ***Transmission electron microscopy (TEM)***

253 Samples were immersed in 2% glutaraldehyde and 2% paraformaldehyde in 100 mM
254 phosphate buffer (PB) for 24 h at 4 °C. They were then postfixed with 2% osmium tetroxide
255 in 100 mM PB for 1.5 h at 4 °C, after which they were rinsed with 100 mM PB, and
256 dehydrated through a graded series of ethanol treatments. They were embedded in Spurr resin
257 (Polysciences Inc., Warrington, PA, USA), cut into ultrathin sections, and stained with uranyl
258 acetate and lead citrate. The ultrathin sections were observed using a Hitachi H-7650 TEM
259 (Hitachi High-Tech Corp., Tokyo, Japan).

260

261 ***Plasmids and purification of recombinant proteins***

262 For recombinant Thiredoxin1 proteins, rat *Txn1* cDNAs were amplified by PCR using
263 LA-Taq polymerase (Takara Bio Inc, Shiga, Japan) with FW-primer: 5'-GGA TCC ATG
264 GTG AAG CTG ATC GAG AG-3'; and RV-primer, 5'- GTC GAC TTA GCT GTC CAT
265 GTG CTG GCG TTC GAA TTT AGC GGT TTC TTT GAA TTC GGC AAA CTC CGT
266 AAT AGT GG-3' (Sigma-Aldrich Japan, Inc., Tokyo, Japan). The PCR products were cloned
267 into a pCMV-Tag2 plasmid (Stratagene, San Diego, CA, USA) digested with *Bam*HI and *Sal*I
268 containing FLAG-tag and S-tag sequences. The DNA sequence of the plasmids was
269 confirmed by DNA sequencing using a BigDye Terminator FS Ready-Reaction Kit (Applied
270 Biosciences, Little Chalfont, Buckinghamshire, UK) and an ABI 3130x Genetic Analyzer
271 (Applied Biosciences). The plasmids were transfected into HEK293 human embryonic kidney
272 cells using Lipofectamine2000 (Invitrogen, Carlsbad, CA, USA). The recombinant proteins
273 were purified with anti-FLAG agarose affinity gel (A2220; Sigma-Aldrich Japan), eluted with
274 FLAG peptide (A3290; Sigma-Aldrich Japan), and filtered using an ultrafiltration membrane
275 (Amicon Ultra 3 K; Millipore, Burlington, MA, USA).

276

277 ***Insulin-reducing activity assay***

278 Thioredoxin activity was measured using a thioredoxin activity assay kit (Redoxica, Little
279 Rock, AR, USA), according to the manufacturer's instructions. In brief, the purified
280 recombinant thioredoxin1 proteins or protein extracts from rat thalamus and cortex were
281 reacted with insulin and NADPH in assay buffer, and thioredoxin activity was determined as
282 a change in the amount of oxidized NADPH by measuring the decrease in absorbance at 340
283 nm per minute using a spectrophotometer DeNovix DS-11 (DeNovix, Tokyo, Japan).

284

285 *Primary fibroblast and neuron culture*

286 Newborn rats were sacrificed under deep anesthesia with isoflurane on the day of birth. The
287 animals were dissected in the surgical suite and disinfected with 70% alcohol. For primary
288 fibroblast culture, the abdominal skin tissues were cut into small pieces in DMEM (Fujifilm
289 Wako Pure Chemical Corporation, Osaka, Japan) and disrupted by pipetting. The cell
290 suspension was transferred and maintained in DMEM supplemented with 10% fetal bovine
291 serum (Thermo Fisher Scientific, Waltham, MA, USA), 500U/ml penicillin, and 500 ug/ml
292 streptomycin (Sigma-Aldrich Japan, Inc., Tokyo, Japan) in a fully humidified atmosphere of
293 5% CO₂. After about two weeks, fibroblast cells were cultured in DMEM supplemented with
294 10% fetal bovine serum, 100U/ml penicillin, and 100 ug/ml streptomycin.

295

296 For primary neuronal culture, we referred to a protocol using a postnatal mouse [23] and
297 modified it. We used the cerebral cortex of rats on the first postnatal day. Tissues were treated
298 with 0.125% trypsin (Thermo Fisher Scientific) and 0.004% DNase-I (Sigma-Aldrich) at
299 37 °C for 15 min and dissociated mechanically. Cells were plated on poly-l-lysine and
300 laminin-coated glass-bottomed 35-mm culture dishes. Cells were maintained in a culture
301 medium with DMEM, 100 µg/ml penicillin-streptomycin (Thermo Fisher Scientific) and 10%
302 fetal calf serum (Thermo Fisher Scientific) at 37 °C in a humidified incubator with 95% air
303 and 5% CO₂. On the second day, the culture medium was replaced with a medium containing

304 DMEM, 2% B-27 supplement (Thermo Fisher Scientific), and 5% fetal calf serum. The
305 culture medium was refed with a medium containing DMEM, α -MEM, F-12 nutrient mixture,
306 2% B-27 supplement, 0.34% glucose, 25 μ M 5-fluoro-deoxyuridine, 25 μ M uridine, one mM
307 kynurenic acid (Sigma-Aldrich), and 1% fetal calf serum on the fourth day. Cultures were
308 used for the experiments on days 9–15. Mitochondria and nuclei were stained using
309 MitoBright LT Red (Dojindo, Kumamoto, Japan) and Cellstain-Hoechst33258 solution
310 (Dojindo, Kumamoto, Japan), respectively.

311

312 *Terminal deoxynucleotidyl transferase (TdT) dUTP Nick-End Labeling (TUNEL) assay*

313 For determining apoptosis, paraffin-embedded brain tissues at three weeks of age and primary
314 fibroblasts were assessed using the In Situ Cell Death Detection Kit, TMR red
315 (Sigma-Aldrich Japan, Inc., Tokyo, Japan), following the manufacturer's instructions. We
316 compared cell death during incubation of primary fibroblasts with and without the addition of
317 300 μ M hydrogen peroxide for 3h. In brief, the cells were cultured on an 8-chamber culture
318 slide (BD Falcon, Franklin Lakes, NJ, USA), washed with phosphate-buffered saline (PBS),
319 fixed with 10% formalin neutral buffer solution (Fujifilm Wako Pure Chemical Corporation,
320 Osaka, Japan) for one h at room temperature, and treated with permeabilization solution for 2
321 min on ice. TMR red-labeled dUTP was incorporated into 3'-OH DNA ends by terminal
322 deoxynucleotidyl transferase, and the fluorescence signal was detected using a BZX-700
323 microscope (Keyence, Osaka, Japan) or a fluorescence microscope (Olympus IX71; Olympus
324 Corporation, Tokyo, Japan).

325

326 *Statistical analysis*

327 Results are expressed as mean \pm SEM. The sample size for each experiment is indicated in the
328 figure and figure legends. One-way analysis of variance (ANOVA) was used to compare
329 between three groups. Statistical significance was set at $p < 0.05$. Bonferroni adjustment was

330 used to determine the statistical differences between the groups. All significant statistical
331 results are indicated within the figures using the following conventions: * $p < 0.05$, ** $p <$
332 0.01 , *** $p < 0.001$.

333

334 **Results**

335 *Discovery of a novel epileptic rat with Txn1 missense mutation*

336 A strain exhibiting unique running seizures was identified in an archive of ENU-mutated rats.
337 Thus, we decided to identify the responsible gene. By analyzing simple sequence length
338 polymorphism (SSLP) markers on mutant ($n = 21$) and sibling ($n = 25$) DNA pools,
339 the *Adem* locus was roughly mapped on chromosomes 2 and 5. The locus was subsequently
340 refined by 26 and 33 SSLP markers for each chromosome, and mapped to a 1.5-Mb genomic
341 region, between markers D5Mit17 (Chr 5: 75,159,412–75,159,546) and D5Rat113 (Chr
342 5:76,707,365–76,707,563) (RGSC_v3.4) (Fig. 1A). Ten known or predicted genes within
343 the *Adem* region
344 (*Ptpn3*, *Palm2*, *AC134204.1*, *Akap2*, *LOC685849*, *Txn1*, *Txndc8*, *Svep1*, *Musk*, *Lpar1*) were
345 identified from the Ensembl database (<http://www.ensembl.org>).

346

347 We performed next-generation sequencing analysis of genomic DNA from 75,159,000 to
348 76,708,000 on Chr5 using the SureSelect target enrichment approach (Agilent). In mutant
349 DNA, we found only one heterozygous missense mutation in the exon region, c. T160C, in
350 exon 3 of the *Txn1* gene (NM_053800, ENSRNOG00000012081.6) by comparing the
351 parental strain F344/NSlc. This variant caused a substitution of phenylalanine for leucine at
352 residue 54 (Fig. 1B).

353

354 Txn1 is widespread in prokaryotes and eukaryotes, and its amino acid sequence is well
355 conserved in mammals (Fig. 1D). Amino acid sequences are 90% identical in humans and rats.
356 Since the structure of rat thioredoxin has not been reported, we plotted the position of F54 on
357 the 3D structure of human thioredoxin (UniProt, <https://www.uniprot.org/>). The positions of
358 amino acids with important functions in Txn1 were plotted on the structure. Txn1 has an
359 active center sequence Cys32-Gly-Pro-Cys35 motif and carries out redox reactions by
360 dithiol/disulfide exchange reactions between Cys32 and Cys35 [24, 25, 26]. Both Cys69 and
361 Cys73 are nitrosylated in response to nitric oxide (NO) [26, 27]. Cys-73 can serve as a donor
362 for the nitrosylation of target proteins. The location of the F54L mutation is remote from these
363 active sites (Fig. 1C and Fig. 1D), suggesting that it is not directly involved in the
364 dithiol/disulfide exchange reaction or S-nitrosylation. However, the PolyPhen-2 prediction
365 (<http://genetics.bwh.harvard.edu/pph2/index.shtml>) found that the F54L mutation is possibly
366 damaging with a score of 0.785, and the Sorting Intolerant From Tolerant (SIFT,
367 <http://www.ngl.org.uk/Manchester/page/sift-sorting-intolerant-tolerant.html>) sequence is
368 deleterious.

369

370 ***Vacuolar degeneration appears during an epileptic period***

371 Video monitoring showed that the frequency of seizures peaks at 5-week of age in both
372 heterozygotes (Fig. 2A) and homozygotes (Fig. 2B). There were no differences in seizure
373 frequencies between heterozygotes and homozygotes.

374

375 Next, a histological examination was performed at five weeks to determine whether a
376 structural change was the cause of epilepsy. Surprisingly, vacuolar degeneration was found in
377 the inferior colliculus and thalamus of the mutants. (Fig. 2C). No changes were observed in
378 the hippocampus, which is prone to epilepsy. Bodian staining, which is used to observe nerve
379 fibers, and Klüver-Barrera (KB) staining, which is used to observe the myelin sheath,

380 exhibited decreased staining in the mutants. These histological tests showed that homozygotes
381 had more severe lesions than heterozygotes. We examined when these lesions had started
382 developing (Fig. 2D). There were no remarkable changes in the inferior colliculus at two
383 weeks of age. However, vacuoles became evident in the inferior colliculus and thalamus at
384 three weeks of age and were then widespread at five weeks of age. They almost disappeared
385 completely after nine weeks.

386

387 ***MRI showed transient high signals of T2-weighted images in the midbrain***

388 MRI detected hyperintense regions of T2-weighted images (T2WI) spread around the
389 thalamus in mutant rats at five weeks of age (Fig. 3A). The hyperintense regions of the
390 heterozygous and homozygous T2WI were symmetrical. The lesions were localized in the
391 thalamus, inferior colliculus, superior colliculus, and hypothalamus in homozygotes (Fig. 3B).
392 The hyperintensity region of T2WI in homozygous rats was wider than that in heterozygous
393 rats (see also Supplementary Fig. S1, S2, and S3). Temporal lesions were also examined using
394 MRI in the same individual. Serial MRI examination revealed that the lesions at three weeks
395 spread or were similar in size at five weeks. However, the lesions shrank at seven weeks and
396 disappeared at nine weeks (Fig. 3C). The weekly changes observed on MRI were similar to
397 those seen in the histological examination.

398

399 ***Neuronal and oligodendrocyte cell loss occurs in the midbrain***

400 Western blotting of the midbrain using NeuN, Olig2, GFAP, and anti-IbaI antibodies showed
401 a decrease in NeuN and Olig2 and an increase in GFAP and IbaI expression in heterozygotes
402 and homozygotes (Fig. 4A). Immunohistochemical studies showed significantly decreased
403 numbers of NeuN-positive neurons (Fig. 4B and 4C) and Olig2-positive oligodendrocytes
404 (Fig. 4D and 4E). NeuN-positive neurons in heterozygotes and homozygotes had larger cell
405 bodies than wild-type (WT) rats. Electron microscopy of the lesions in the mutant rats

406 revealed that microtubules in the vacuoles and myelin sheath were wrapped around the
407 vacuoles (Fig. 4H and 4I). These findings indicate that the vacuoles were dilated axons of the
408 neurons. Examination of the mitochondrial morphology showed sparse cristae in the mutant,
409 even though the neurons retained their structures (Fig. 4J and 4 K).

410

411 ***Txn1-F54L shows decreased insulin-reducing activity***

412 Fig. 5A shows the thioredoxin/peroxiredoxin system. Four central enzyme systems defend
413 against oxidative stress by scavenging ROS generated in the body. These include SOD, which
414 scavenges superoxide, CAT, GPx, and thioredoxin-dependent peroxiredoxin (Prdx).
415 Thioredoxin forms a system with nicotinamide adenine dinucleotide phosphate (NADPH) and
416 thioredoxin reductase (Txnrd) to reduce disulfide bonds in target proteins. Thioredoxin is
417 responsible for converting the target protein from oxidized to the reduced form and
418 scavenging H₂O₂ via Prdx. To confirm whether the reduced expression of Txn1 underlies the
419 changes in the brain during 3–5 weeks of age, we examined the expression level of Txn1
420 protein in the brain, kidney, heart, and liver by western blotting at four weeks of age when
421 vacuoles appeared and at 16 weeks of age when repair occurred. We found that Txn1 was
422 equally expressed in all organs, and there was no change between 4 and 16 weeks of age (Fig.
423 5B).

424

425 Next, we measured thioredoxin activity by using recombinant protein (Fig. 5C), the thalamus
426 at five weeks of age, where vacuolar degeneration was observed (Fig. 5D), and the frontal
427 cortex (Fig. 5E), where vacuolar degeneration did not occur. Our results showed that the
428 insulin-reducing activity of *Txn1-F54L* was decreased to approximately one-third of that of
429 the WT. Similarly, insulin-reduction activity in the thalamus was reduced in heterozygotes
430 and reduced much further in homozygotes compared to that in WT mice (Fig. 5D).

431 Interestingly, reduced activity was also observed in the cortex, where there was no vacuolar
432 degeneration (Fig. 5E).

433

434 ***Oxidative damage in the midbrain and susceptibility to cell death under oxidative stress***

435 Next, we investigated the pathogenesis underlying the vacuolar degeneration. Staining with
436 8-OHdG, which indicates oxidative stress-induced DNA damage, and 4-HNE, which
437 indicates lipid oxidation, showed brain staining in the mutant lesions (Fig. 6A). The area of
438 8-OHdG (Fig. 6B) and 4-HNE (Fig. 6C) positive cells were significantly increased in
439 heterozygous and homozygous rats compared to WT cells. TUNEL assay of
440 paraffin-embedded sections, including the thalamus, showed slight staining in heterozygous
441 and homozygous rats at three weeks of age (Fig. 6D). Next, we examined cellular
442 vulnerability to H₂O₂ using primary fibroblasts and cortical neurons derived from WT and
443 homozygous rats. The TUNEL assay showed that homozygous fibroblasts were slightly
444 stained even under standard culture medium, and the staining became significantly stronger
445 when H₂O₂ was added. In contrast, TUNEL-positive cells in WT fibroblasts did not increase
446 with the addition of 0.3 mM H₂O₂ (Fig. 6E). We also found that WT primary neurons showed
447 no significant changes, whereas homozygous neurons showed cell death and nuclear rupture
448 on treatment with 0.3 mM H₂O₂ (Fig. 6F).

449

450 ***Txn1-F54L rat generated by genome editing replicates vacuolar degeneration in the*** 451 ***midbrain***

452 Finally, we conducted reproducibility experiments to confirm whether the *Txn1*-F54L
453 mutation is the sole cause of the F344/NSlc phenotype. Genome editing using CRISPR-Cas9
454 was used to generate F344/Jcl rats with the *Txn1*-F54L mutation. We placed 5-week-old
455 F344/Jcl *Txn1*-F54L heterozygous rats under 24-hour video monitoring and recorded running
456 seizures eight times/24 h (a total of N = 5) (Supplementary Video 2). Running seizures and

457 transition from running to tonic seizures were observed. These seizure symptoms were similar
458 to those observed in *Adem* rats harboring *Txn1*-F54L. The lesions were localized in the
459 thalamus, hypothalamus, and superior and inferior colliculi and were more extensive in
460 homozygous than in heterozygous rats (Fig. 7A and 7 B). The vacuoles in the midbrain
461 started developing at two weeks of age, became apparent at three weeks, and recovered at
462 nine weeks (Supplementary figure 4). Although the genetic background of F344/NSlc
463 generated by ENU-mutagenesis and F344/Jcl is somewhat different, transient vacuolar
464 degeneration localized in the midbrain was reproduced in F344/Jcl rats carrying the *Txn1*-
465 F54L mutation.

466

467 **Discussion**

468 The function of TXN in vivo remains unclear. *Txn1* is located in the cytoplasm, nucleus, and
469 extracellular region [25, 28], whereas *Txn2* is located in the mitochondria [29]. A
470 homozygous *TXN2* mutation has been linked to an infantile-onset neurodegenerative disorder
471 with severe cerebellar and optic atrophy and peripheral neuropathy [30]. To the best of our
472 knowledge, there are no reports of *TXN1* mutations that cause human diseases. Herein, we
473 discovered a link between *Txn1* mutations and CNS disorders in mammals for the first time.
474 The loss of *Txn1* function leads to neuronal death with abnormal mitochondrial structure in
475 the midbrain.

476 *Txnrd* catalyzes the reduction of oxidized *Txn* in an NADPH-dependent manner. Genetically
477 modified mice with inactivation of *Txnrd1* or *Txnrd2* show embryonic lethality [31, 32], so
478 the *Txn*/*Txnrd* systems have not been elucidated in vivo beyond the fact that they are
479 essential for fetal development. Other important interacting proteins include the *Prdx* family,
480 which scavenges H₂O₂. Knockout mice for *Prdx1*, *Prdx2*, *Prdx3*, *Prdx4*, or *Prdx5* exhibited
481 various kinds of disorders such as hemolytic anemia, metabolic abnormalities, inflammation,

482 cancer, and age-related phenotypes [33]. The discovery of *Adem* rats may shed light on new
483 roles of the Txn/ Txnrd systems and Txn/ Prdx systems.

484

485 *Adem* rats exhibited running seizures and a transition from running to tonic seizures. The
486 focus on this unique epileptic seizure has led to a significant discovery. Running seizures are
487 rarely reported as symptoms of epileptic seizures. According to reports from the 1980s and
488 the 1990s, electrical stimulation of the inferior colliculus and midbrain reticular formation [34,
489 35, 36] or intense acoustic stimulation [37] induced running seizures. In addition, some
490 evoked running seizures are followed by tonic seizures [35, 36, 37]. The seizure symptoms in
491 the *Adem* rats share similarities with these symptoms. The time of spontaneous appearance
492 and suppression of epileptic seizures and the time of onset and repair of the midbrain lesion
493 were almost the same. This suggests that the cause of epilepsy is a midbrain lesion involving
494 the inferior colliculus and thalamus.

495

496 Upon observing the unique vacuolar degeneration in the midbrain of *Adem* rats, we had
497 several questions. First, is there a reduction in cell number in the midbrain? Second, is there
498 an alteration in the reducing activity of *Txn1-F54L*? Third, are the cells derived
499 from *Adem* rats more prone to cell death in response to excess ROS? Fourth, why are
500 vacuoles confined to the midbrain at 3–5 weeks of age? We have discussed our findings based
501 on these questions below.

502

503 Western blotting and immunohistochemistry showed a reduction in both neurons and
504 oligodendrocytes in the *Adem* rats. The cell bodies of NeuN-positive cells were more
505 significant than in the WT, and pronounced axon swelling was identified by TEM. These
506 findings suggest that vacuoles are involved in neuronal and oligodendrocyte cell death.

507 Neuronal activity controls oligodendrocyte development and myelination [38, 39, 40], and

508 neuronal cell death inhibits myelination. Further, as neurons and oligodendrocytes are closely
509 related during development, cell death can occur.

510

511 Our recombinant protein assay showed that the insulin-reducing activity in the mutant rats
512 decreased to approximately one-third that of the WT. In addition, reduced enzymatic activity
513 was observed in the thalamus, where there was a lesion, and in the cortex, where no lesion
514 was present. F54L is located far from the CGPC motif, which plays a central role in TXN
515 activity. However, PolyPhen-2 and SIFT predicted that the F54L mutation was a
516 loss-of-function mutation. The missense mutation may cause a structural change in the region
517 where the dithiol/disulfide exchange reaction occurs.

518

519 In primary cultured neurons and fibroblasts derived from *Adem* rats, cell death was induced
520 more readily than in the WT in the culture medium with H₂O₂. IHC with 8-OHdG and 4-HNE,
521 and TUNEL assays stained more intensely in the brain lesions in *Adem* rats than in the WT.
522 These results suggest that the cells in *the Adem* rats are vulnerable to excessive ROS. Txn1
523 has anti-apoptotic functions in various cells [41, 42, 43]. Loss of function of Txn1 can cause
524 cell death [44, 45, 46]. Proteins that are associated with apoptosis through interaction with
525 Txn1 include apoptosis signal-regulating kinase 1 (ASK1) [47, 48] and Caspase-3 (CASP3)
526 [49]. In addition to apoptosis, other mechanisms of neuronal death could be involved, such as
527 phagocytosis, pyroptosis, and ferroptosis [50]. Western blotting of 5-week-old brains showed
528 a dense band reacting to anti-Iba1 antibody, suggesting an increase in microglia. Microglial
529 activation is a common feature of neurodegenerative diseases. Activated microglia have been
530 reported to kill neurons by releasing TNF- α , glutamate, reactive oxygen, and nitrogen species,
531 which can cause apoptosis, excitotoxicity, and necrotic death of surrounding neurons [51, 52].

532

533 Our results could not clearly determine why the midbrain vacuoles were confined to 3–5
534 weeks of age. The *Txn1* gene is ubiquitously expressed throughout the body (*TXN* thioredoxin
535 [Homo sapiens (human)] - Gene - NCBI <https://www.ncbi.nlm.nih.gov/gene/7295>). Western
536 blotting of *Adem* rats also showed that thioredoxin was expressed in several organs other than
537 the brain. The insulin-reducing activity of thioredoxin was reduced to one-third of that of the
538 WT, both in the thalamus, where vacuolar degeneration appeared, and in the cerebral cortex,
539 where vacuolar degeneration did not appear. Furthermore, *Adem* rat-derived primary cultured
540 fibroblasts and neurons showed a similar level of cell death induced by excessive ROS. These
541 results of *in vitro* experiments indicate that cell death can be caused by excessive ROS,
542 regardless of the cell type, under the same cell culture conditions. The curious phenomenon of
543 limited onset of neuronal death in the midbrain may be due to the location- and age-specific
544 microenvironment of the midbrain. For example, the neurodevelopmental stage at 3–5 weeks
545 of age might trigger an increased mitochondrial ROS leakage due to high glucose metabolism
546 in the midbrain. The F54L mutation-specific inability of *Txn1* to reduce essential proteins for
547 maintaining ROS homeostasis in the midbrain or the dependence of the midbrain region on
548 the thioredoxin/peroxiredoxin antioxidant system might be high. The
549 thioredoxin/peroxiredoxin system, and not the glutathione system, was reported to be a
550 significant contributor to mitochondrial H₂O₂ removal in the brain [53].

551

552 Another surprising phenomenon in *Adem* rats is that repair of the vacuolar lesions can already
553 be seen at seven weeks on MRI, and they are almost entirely repaired at nine weeks. Both
554 astrocytes and microglia have been reported to be involved in cytotoxicity and tissue repair.
555 Astrocytes have long been thought to inhibit neuronal repair, but it has been noted that glial
556 activation induces neurogenesis and acts in repair [54, 55]. Microglia phagocytose and
557 remove debris and dead neurons, and release BDNF and IGF to repair damage to neurons [56,
558 57, 58]. In vacuolar lesions, glial cells may play roles in repair and impart neuropathic effects,

559 or their roles may change from damage to repair. Although this is an exciting point, it is far
560 from the purpose of this study, which was to identify a causative gene of epilepsy and clarify
561 the underlying pathology. We will study this in the future.

562

563 We have not yet identified the precise functions disturbed by Txn1-F54L because Txn1
564 interacts with a wide variety of proteins [59, 60, 61]. This is a limitation of this study.

565 Oxidative stress is responsible for many neurodegenerative diseases [2, 3, 4] and cerebral
566 ischemic-reperfusion injury [62, 63]. The vacuolar degeneration in *Adem* rats may share a
567 common pathological pathway with these neurological disorders. If a common pathway is
568 identified, *Adem* rats would be an attractive animal model. New therapeutic agents for
569 oxidative stress-related diseases can be evaluated more easily because neuronal death occurs
570 spontaneously in a short time and does not require surgical treatment.

571

572 **Conclusions**

573 We have shown that the *Txn1*-F54L mutation confers epilepsy. The underlying pathology
574 of *Adem* rats with *Txn1*-F54L is the loss of neurons and oligodendrocytes in the midbrain.
575 *Txn1*-F54L had a reduced insulin-reducing activity compared to that of the WT. Primary
576 cultured cells, both fibroblasts and neurons, derived from *Adem* rats exhibited cell death under
577 excess H₂O₂. The mutation might be affecting the midbrain microenvironment in a specific
578 manner leading to the death of neurons and oligodendrocytes in that region. Further studies
579 are required to determine this midbrain-specific function of Txn1.

580

581 **Author contributions**

582 T.M discovered the *Adem* rat; I.O. and M.O. performed the phenotypic characterization of this
583 strain; T.M. and S.I. created the genome-edited mutant rats; H.I. supervised the MRI
584 examination and analyzed the data; S.T. supervised the histopathological experiments;
585 Conceptualization, I.O., M.O., and T. M.; Investigation, I.O., M.O., H.I., S.I., S.T., and T.M.;
586 Writing – Original Draft, I.O.; Writing – Review & Editing, M.O. H.I., S.I., S.T., and T. M.;
587 Project Administration, I.O.; Funding Acquisition, M.O., I.O., and T.M. All authors approved
588 the final manuscript.

589

590 **Declaration of competing interest**

591 The authors declare no competing financial interests.

592

593 **Acknowledgments**

594 We thank Ms. Yumiko Morishita, Mika Monobe, and Miki Kajino for technical assistance
595 with histology and IHC. We thank Ms. Masumi Hurutani for the technical assistance with EM.
596 This work was supported by Grants-in-Aid for Scientific Research (16H05354), Grant-in-Aid
597 for epilepsy research from the Japan Epilepsy Research Foundation, and JSPS KAKENHI
598 Grant Number JP16H06276 (AdAMS).

599 We would like to thank Editage (www.editage.com) for English language editing.

600 **References**

- 601 1. Dringen R. Metabolism and functions of glutathione in brain. *Prog Neurobiol.* 2000
602 Dec;62(6):649-71. doi: 10.1016/s0301-0082(99)00060-x.
- 603 2. Lin MT, Beal MF. Mitochondrial dysfunction and oxidative stress in neurodegenerative
604 disease *Nature.* 2006 Oct 19;443(7113):787-95. doi: 10.1038/nature05292.
- 605 3. Uttara B, Singh AV, Zamboni P, Mahajan RT. Oxidative stress and neurodegenerative
606 diseases: a review of upstream and downstream antioxidant therapeutic options. *Curr*
607 *Neuropharmacol.* 2009 Mar;7(1):65-74. doi: 10.2174/157015909787602823.

- 608 4. Elfawy HA, Das B. Crosstalk between mitochondrial dysfunction, oxidative stress, and age
609 related neurodegenerative disease: Etiologies and therapeutic strategies. *Life Sci.* 2019 Feb
610 1;218:165-184. doi: 10.1016/j.lfs.2018.12.029. Epub 2018 Dec 20.
- 611 5. Nathan C, Cunningham-Bussell A. Beyond oxidative stress: an immunologist's guide to
612 reactive oxygen species. *Nat Rev Immunol.* 2013 May;13(5):349-61. doi: 10.1038/nri3423.
- 613 6. Dan Dunn J, Alvarez LA, Zhang X, Soldati T. Reactive oxygen species and mitochondria:
614 A nexus of cellular homeostasis. *Redox Biol.* 2015 Dec;6:472-485. doi:
615 10.1016/j.redox.2015.09.005. Epub 2015 Sep 10.
- 616 7. Sarniak A, Lipińska J, Tytman K, Lipińska S. Endogenous mechanisms of reactive oxygen
617 species (ROS) generation. *Postepy Hig Med Dosw (Online).* 2016 Nov 14;70(0):1150-1165.
618 doi: 10.5604/17322693.1224259.
- 619 8. Dröge W. Free radicals in the physiological control of cell function. *Physiol Rev.* 2002
620 Jan;82(1):47-95. doi: 10.1152/physrev.00018.2001.
- 621 9. Laurent TC, Moore EC, Reichard P. Enzymatic synthesis of deoxyribonucleotides. Iv.
622 Isolation and characterization of thioredoxin, the hydrogen donor from *Escherichia coli* B. *J*
623 *Biol Chem.* 1964 Oct;239:3436-44.
- 624 10 . Wakasugi N, Tagaya Y, Wakasugi H, Mitsui A, Maeda M, Yodoi J, Tursz T. Adult T-cell
625 leukemia-derived factor/thioredoxin, produced by both human T-lymphotropic virus type I-
626 and Epstein-Barr virus-transformed lymphocytes, acts as an autocrine growth factor and
627 synergizes with interleukin 1 and interleukin 2. *Proc Natl Acad Sci U S A.* 1990
628 Nov;87(21):8282-6. doi: 10.1073/pnas.87.21.8282.
- 629 11. Baker, A., Payne, C. M., Briehl, M. M. & Powis, G. Thioredoxin, a gene found
630 overexpressed in human cancer, inhibits apoptosis *in vitro* and *in vivo*. *Cancer Res.* 1997 Nov
631 15;57(22):5162-7.
- 632 12. Lincoln DT, Ali Emadi EM, Tonissen KF, Clarke FM. The thioredoxin-thioredoxin
633 reductase system: over-expression in human cancer. *Anticancer Res.* 2003
634 May-Jun;23(3B):2425-33.
- 635 13. Harris IS, Treloar AE, Inoue S, Sasaki M, Gorrini C, Lee KC, Yung KY, Brenner D,
636 Knobbe-Thomsen CB, Cox MA, Elia A, Berger T, Cescon DW, Adeoye A, Brüstle A,
637 Molyneux SD, Mason JM, Li WY, Yamamoto K, Wakeham A, Berman HK, Khokha R, Done
638 SJ, Kavanagh TJ, Lam CW, Mak TW. Glutathione and thioredoxin antioxidant pathways

- 639 synergize to drive cancer initiation and progression. *Cancer Cell*. 2015 Feb 9;27(2):211-22.
640 doi: 10.1016/j.ccell.2014.11.019.
- 641 14. Zhang J, Li X, Han X, Liu R, Fang J. Targeting the Thioredoxin System for Cancer
642 Therapy. *Trends Pharmacol Sci*. 2017 Sep;38(9):794-808. doi: 10.1016/j.tips.2017.06.001.
- 643 15. Ghareeb H, Metanis N. The Thioredoxin System: A Promising Target for Cancer Drug
644 Development. *Chemistry*. 2020 Aug 12;26(45):10175-10184. doi: 10.1002/chem.201905792.
- 645 16. Yamamoto M, Yang G, Hong C, Liu J, Holle E, Yu X, Wagner T, Vatner SF, Sadoshima
646 J Inhibition of endogenous thioredoxin in the heart increases oxidative stress and cardiac
647 hypertrophy. *J Clin Invest*. 2003 Nov;112(9):1395-406. doi: 10.1172/JCI17700.
- 648 17. Matsui M, Oshima M, Oshima H, Takaku K, Maruyama T, Yodoi J, Taketo MM. Early
649 embryonic lethality caused by targeted disruption of the mouse thioredoxin
650 gene. *Developmental Biology*. 1996;178(1):179-185.
- 651 18. Mashimo T, Yanagihara K, Tokuda S, Voigt B, Takizawa A, Nakajima R, Kato M,
652 Hirabayashi M, Kuramoto T, Serikawa T. An ENU-induced mutant archive for gene targeting
653 in rats. *Nat Genet*. 2008 May;40(5):514-5. doi: 10.1038/ng0508-514.
- 654 19. Serikawa T, Mashimo T, Takizawa A, Okajima R, Maedomari N, Kumafuji K, Tagami F,
655 Neoda Y, Otsuki M, Nakanishi S, Yamasaki K, Voigt B, Kuramoto T. National BioResource
656 Project-Rat and related activities. *Exp Anim*. 2009 Jul;58(4):333-41.
- 657 20. Ishida S, Sakamoto Y, Nishio T, Baulac S, Kuwamura M, Ohno Y, Takizawa A, Kaneko
658 S, Serikawa T, Mashimo T. Kcna1-mutant rats dominantly display myokymia, neuromyotonia
659 and spontaneous epileptic seizures. *Brain Res*. 2012 Jan 30;1435:154-66.
- 660 21. Yoshimi K, Kunihiro Y, Kaneko T, Nagahora H, Voigt B, Mashimo T. ssODN-mediated
661 knock-in with CRISPR-Cas for large genomic regions in zygotes. *Nat Commun*. 2016 Jan
662 20;7:10431. doi: 10.1038/ncomms10431.
- 663 22. Miyasaka Y, Uno Y, Yoshimi K, Kunihiro Y, Yoshimura T, Tanaka T, Ishikubo H,
664 Hiraoka Y, Takemoto N, Tanaka T, Ooguchi Y, Skehel P, Aida T, Takeda J, Mashimo T.
665 CLICK: one-step generation of conditional knockout mice. *BMC Genomics*. 2018 May
666 2;19(1):318. doi: 10.1186/s12864-018-4713-y.
- 667 23. Beaudoin GM 3rd, Lee SH, Singh D, Yuan Y, Ng YG, Reichardt LF, Arikath J.
668 Culturing pyramidal neurons from the early postnatal mouse hippocampus and cortex. *Nat*
669 *Protoc*. 2012 Sep;7(9):1741-54. doi: 10.1038/nprot.2012.099.

- 670 24. Lu J, Holmgren A. The thioredoxin antioxidant system. *Free Radic Biol Med.* 2014
671 Jan;66:75-87. doi: 10.1016/j.freeradbiomed.2013.07.036.
- 672 25. Kang Z, Qin T, Zhao Z. Thioredoxins and thioredoxin reductase in chloroplasts: A review
673 *Gene.* 2019 Jul 20;706:32-42. doi: 10.1016/j.gene.2019.04.041.
- 674 26. Hirota K, Matsui M, Iwata S, Nishiyama A, Mori K, Yodoi J. AP-1 transcriptional activity
675 is regulated by a direct association between thioredoxin and Ref-1 *Proc Natl Acad Sci U S A.*
676 1997 Apr 15;94(8):3633-8. doi: 10.1073/pnas.94.8.3633.
- 677 27. S-nitrosation of procaspase-3 and the inhibition of apoptosis in Jurkat cells *Proc Natl*
678 *Acad Sci U S A.* 2007 Jul 10;104(28):11609-14. doi: 10.1073/pnas.0704898104.
- 679 28. Rubartelli A, Bajetto A, Allavena G, Wollman E, Sitia R. Secretion of thioredoxin by
680 normal and neoplastic cells through a leaderless secretory pathway. *J Biol Chem.* 1992 Dec
681 5;267(34):24161-4.
- 682 29. Spyrou G, Enmark E, Miranda-Vizuete A, Gustafsson J. Cloning and expression of a
683 novel mammalian thioredoxin. *J Biol Chem.* 1997 Jan 31;272(5):2936-41. doi:
684 10.1074/jbc.272.5.2936.
- 685 30. Holzerova E, Danhauser K, Haack TB, Kremer LS, Melcher M, Ingold I, Kobayashi S,
686 Terrile C, Wolf P, Schaper J, Mayatepek E, Baertling F, Friedmann Angeli JP, Conrad M,
687 Strom TM, Meitinger T, Prokisch H, Distelmaier F. Human thioredoxin 2 deficiency impairs
688 mitochondrial redox homeostasis and causes early-onset neurodegeneration. *Brain.* 2016
689 Feb;139(Pt 2):346-54. doi: 10.1093/brain/awv350.
- 690 31. Jakupoglu C, Przemeck GK, Schneider M, Moreno SG, Mayr N, Hatzopoulos AK, de
691 Angelis MH, Wurst W, Bornkamm GW, Brielmeier M, Conrad M. Cytoplasmic thioredoxin
692 reductase is essential for embryogenesis but dispensable for cardiac development. *Mol Cell*
693 *Biol.* 2005 Mar;25(5):1980-8. doi: 10.1128/MCB.25.5.1980-1988.2005.
- 694 32. Conrad M, Jakupoglu C, Moreno SG, Lippl S, Banjac A, Schneider M, Beck H,
695 Hatzopoulos AK, Just U, Sinowatz F, Schmahl W, Chien KR, Wurst W, Bornkamm GW,
696 Brielmeier M. Essential role for mitochondrial thioredoxin reductase in hematopoiesis, heart
697 development, and heart function. *Mol Cell Biol.* 2004 Nov;24(21):9414-23. doi:
698 10.1128/MCB.24.21.9414-9423.2004.
- 699 33. Lee YJ. Knockout Mouse Models for Peroxiredoxins. *Antioxidants (Basel).* 2020 Feb
700 22;9(2):182. doi: 10.3390/antiox9020182.

- 701 34. McCown TJ, Greenwood RS, Frye GD, Breese GR. Electrically elicited seizures from the
702 inferior colliculus: a potential site for the genesis of epilepsy? *Exp Neurol*. 1984
703 Dec;86(3):527-42. doi: 10.1016/0014-4886(84)90087-6.
- 704 35. Hirsch E, Maton B, Vergnes M, Depaulis A, Marescaux C. Reciprocal positive transfer
705 between kindling of audiogenic seizures and electrical kindling of inferior colliculus. *Epilepsy*
706 *Res*. 1993 Jun;15(2):133-9. doi: 10.1016/0920-1211(93)90093-m.
- 707 36. Maton B, Vergnes M, Hirsch E, Marescaux C. Involvement of proprioceptive feedback in
708 brainstem-triggered convulsions. *Epilepsia*. 1997 May;38(5):509-15. doi:
709 10.1111/j.1528-1157.1997.tb01133.x.
- 710 37. Marescaux C, Vergnes M, Kiesmann M, Depaulis A, Micheletti G, Warter JM. Kindling
711 of audiogenic seizures in Wistar rats: an EEG study. *Exp Neurol*. 1987 Jul;97(1):160-8. doi:
712 10.1016/0014-4886(87)90290-1.
- 713 38. Fields RD. A new mechanism of nervous system plasticity:
714 activity-dependent myelination. *Nat Rev Neurosci*. 2015 Dec;16(12):756-67. doi:
715 10.1038/nrn4023.
- 716 39. Foster AY, Bujalka H, Emery B. Axoglial interactions in myelin plasticity: Evaluating the
717 relationship between neuronal activity and oligodendrocyte dynamics. *Glia*. 2019
718 Nov;67(11):2038-2049. doi: 10.1002/glia.23629.
- 719 40. Pease-Raissi SE, Chan JR. Building a (w)rapport between neurons and oligodendroglia:
720 Reciprocal interactions underlying adaptive myelination. *Neuron*. 2021 Apr
721 21;109(8):1258-1273. doi: 10.1016/j.neuron.2021.02.003.
- 722 41. Baker A, Payne CM, Briehl MM, Powis G. Thioredoxin, a gene found overexpressed in
723 human cancer, inhibits apoptosis *in vitro* and *in vivo*. *Cancer Res*. 1997 Nov
724 15;57(22):5162-7.
- 725 42. Andoh T, Chock PB, Chiueh CC. The roles of thioredoxin in protection against oxidative
726 stress-induced apoptosis in SH-SY5Y cells. *J Biol Chem*. 2002 Mar 22;277(12):9655-60. doi:
727 10.1074/jbc.M110701200.
- 728 43. Haendeler J, Hoffmann J, Tischler V, Berk BC, Zeiher AM, Dimmeler S. Redox
729 regulatory and anti-apoptotic functions of thioredoxin depend on S-nitrosylation at cysteine
730 69. *Nat Cell Biol*. 2002 Oct;4(10):743-9. doi: 10.1038/ncb851.

- 731 44. Tonissen KF, Di Trapani G.
732 Thioredoxin system inhibitors as mediators of apoptosis for cancer therapy. *Mol Nutr Food*
733 *Res.* 2009 Jan;53(1):87-103. doi: 10.1002/mnfr.200700492.
- 734 45. Circu ML, Aw TY. Reactive oxygen species, cellular redox systems, and apoptosis. *Free*
735 *Radic Biol Med.* 2010 Mar 15;48(6):749-62. doi: 10.1016/j.freeradbiomed.2009.12.022.
- 736 46. Benhar M. Oxidants, Antioxidants and Thiol Redox Switches in the Control of Regulated
737 Cell Death Pathways. *Antioxidants (Basel).* 2020 Apr 11;9(4):309. doi:
738 10.3390/antiox9040309.
- 739 47. Saitoh M, Nishitoh H, Fujii M, Takeda K, Tobiume K, Sawada Y, Kawabata M,
740 Miyazono K, Ichijo H. Mammalian thioredoxin is a direct inhibitor of apoptosis
741 signal-regulating kinase (ASK) 1. *EMBO J.* 1998 May 1;17(9):2596-606. doi:
742 10.1093/emboj/17.9.2596.
- 743 48. Tobiume K, Matsuzawa A, Takahashi T, Nishitoh H, Morita K, Takeda K, Minowa O,
744 Miyazono K, Noda T, Ichijo H. ASK1 is required for sustained activations of JNK/p38 MAP
745 kinases and apoptosis. *EMBO Rep.* 2001 Mar;2(3):222-8. doi: 10.1093/embo-reports/kve046.
- 746 49. Mitchell DA, Marletta MA. Thioredoxin catalyzes the S-nitrosation of the caspase-3
747 active site cysteine. *Nat Chem Biol.* 2005 Aug;1(3):154-8. doi: 10.1038/nchembio720. Epub
748 2005 Jul 10.
- 749 50. Fricker M, Tolkovsky AM, Borutaite V, Coleman M, Brown GC. Neuronal cell death.
750 *Physiol Rev.* 2018 Apr 1;98(2):813-880. doi: 10.1152/physrev.00011.2017.
- 751 51. Block ML, Zecca L, Hong JS. Microglia-mediated neurotoxicity: uncovering the
752 molecular mechanisms. *Nat Rev Neurosci* 8: 57–69, 2007. doi:10.1038/nrn2038.
- 753 52. Brown GC, Vilalta A. How microglia kill neurons. *Brain Res* 1628, Pt B: 288–297, 2015.
754 doi:10.1016/j.brainres.2015.08.031.
- 755 53. Drechsel DA, Patel M. Respiration-dependent H₂O₂ removal in brain mitochondria via the
756 thioredoxin/peroxiredoxin system. *J Biol Chem.* 2010 Sep 3;285(36):27850-8.
- 757 54. Silver J, Miller JH. Regeneration beyond the glial scar. *Nat Rev Neurosci.* 2004
758 Feb;5(2):146-56. doi: 10.1038/nrn1326.
- 759 55. Rolls A, Shechter R, Schwartz M. The bright side of the glial scar in CNS repair. *Nat Rev*
760 *Neurosci.* 2009 Mar;10(3):235-41. doi: 10.1038/nrn2591.

- 761 56. Nayak D, Roth TL, McGavern DB. Microglia development and function. *Annu Rev*
762 *Immunol.* 2014;32:367-402. doi: 10.1146/annurev-immunol-032713-120240.
- 763 57. Colonna M, Butovsky O. Microglia Function in the Central Nervous System During
764 Health and Neurodegeneration. *Annu Rev Immunol.* 2017 Apr 26;35:441-468.
- 765 58. Bohlen CJ, Friedman BA, Dejanovic B, Sheng M. Microglia in Brain Development,
766 Homeostasis, and Neurodegeneration. *Annu Rev Genet.* 2019 Dec 3;53:263-288.
- 767 59. Kumar JK, Tabor S, Richardson CC. Proteomic analysis of thioredoxin-targeted proteins
768 in *Escherichia coli*. *Proc Natl Acad Sci U S A.* 2004 Mar 16;101(11):3759-64.
- 769 60. Fu C, Liu T, Parrott AM, Li H. Identification of thioredoxin target protein networks in
770 cardiac tissues of a transgenic mouse. *Methods Mol Biol.* 2013;1005:181-97.
- 771 61. Carrari F, Nunes-Nesi A, Buchanan BB, Reichheld JP, Araújo WL, Fernie AR.
772 Thioredoxin, a master regulator of the tricarboxylic acid cycle in plant mitochondria. *Proc*
773 *Natl Acad Sci U S A.* 2015 Mar 17;112(11):E1392-400.
- 774 62. Allen CL, Bayraktutan U. Oxidative stress and its role in the pathogenesis of ischaemic
775 stroke. *Int J Stroke.* 2009 Dec;4(6):461-70. doi: 10.1111/j.1747-4949.2009.00387.x.
- 776 63. Orellana-Urzúa S, Rojas I, Líbano L, Rodrigo R. Pathophysiology of Ischemic Stroke:
777 Role of Oxidative Stress. *Curr Pharm Des.* 2020;26(34):4246-4260. doi:
778 10.2174/1381612826666200708133912.
- 779

780 **Figure legends**

781 **Fig. 1.** Discovery of a novel epileptic rat with a *Txn1* missense mutation.

782 (A) *Adem* locus mapped to a 1.5-Mb genomic region, between markers D5Mit17 and

783 D5Rat113.

784 (B) DNA sequencing exhibiting c. T160C in exon 3 of the *Txn1* gene, causing a substitution

785 of phenylalanine for leucine at residue 54.

786 (C) Functional sites and F54 were plotted in the 3D structure of human thioredoxin.

787 (D) Alignments of the sequence of *Txn1* gene in mammals.

788

789 **Fig. 2.** Vacuolar degeneration appears during an epileptic period.

790 (A) Total seizure frequency of heterozygotes at each week (N = 8).

791 (B) Total seizure frequency of homozygotes at each week (N = 9).

792 (C) Histology at five weeks of age. At least three animals of each genotype were examined.

793 (D) The representative changes of inferior colliculus lesions from 2 to 9 weeks of age for each

794 genotype.

795

796 **Fig. 3.** MRI demonstrates transient high signals of T2-weighted images in the midbrain.

797 (A) The representative MRI findings at five weeks for each genotype (sagittal slices).

798 (B) The coronal slices of homozygotes at five weeks.

799 (C) The temporal changes of the brain lesion for each genotype from three to nine weeks.

800

801 **Fig. 4.** Neuronal and oligodendrocyte cell loss occurs in the midbrain.

802 (A) Protein levels of each cell in the midbrain at five weeks. Anti-NeuN, anti-Olig2,

803 anti-GFAP, and Iba1 bodies are markers of neurons, oligodendrocytes, astrocytes, and

804 microglia.

805 (B) IHC of the anti-NeuN-positive cells in the inferior colliculus for each genotype.

806 (C) Quantification of NeuN-positive cells. Quantification was performed by assessing five
807 randomly selected fields in the inferior colliculus and thalamus for each genotype.

808 (D) IHC of Olig2-positive cells in the inferior colliculus for each genotype.

809 (E) Quantification of Olig2-positive cells. Quantification was performed by assessing five
810 randomly selected fields in the inferior colliculus and thalamus for each genotype.

811 (F) Representative TEM image in the inferior colliculus of WT rat at four weeks.

812 (G) Magnification of the axon in (F). The yellow arrowhead indicates myelin sheath.

813 (H) Representative TEM image of the synapse in the inferior colliculus of WT rat at four
814 weeks. The yellow arrowhead indicates mitochondria with normal morphology, and the red
815 arrowhead indicates postsynaptic density, corresponding with the synaptic terminal.

816 (I) Magnification of the vacuole in (H). The yellow arrowhead indicates the myelin sheath,
817 and the red arrowhead indicates a microtubule.

818 (J) Representative TEM image of the axon in the midbrain of the heterozygous rat at four
819 weeks. The yellow arrowhead indicates mitochondria with sparse cristae.

820 (K) Representative TEM image of the synapse in the inferior colliculus of WT rat at four
821 weeks. The yellow arrowhead indicates mitochondria with sparse cristae, and the red
822 arrowhead indicates postsynaptic density.

823

824 **Fig.5.** *Txn1*-F54L shows decreased insulin-reducing activity.

825 (A) Thioredoxin/peroxiredoxin system.

826 (B) Protein level of thioredoxin in the brain, kidney, heart, and liver.

827 (C) Insulin-reducing activity determined using recombinant proteins.

828 (D) Insulin-reducing activity of the thalamus for each genotype.

829 (E) Insulin-reducing activity of the cortex for each genotype.

830

831 **Fig. 6.** Oxidative damage in the midbrain and susceptibility to cell death under oxidative
832 stress.
833 (A) Oxidative damage in the midbrain was assessed by IHC using anti-8-OHdG antibody and
834 4-HNE.
835 (B) Quantification of 8-OHdG-positive cells for each genotype.
836 (C) Quantification of 4-HNE-positive cells for each genotype.
837 (D) TUNEL assay of the paraffin-embedded sections including thalamus for each genotype.
838 (E) TUNEL assay of the primary fibroblasts derived from the WT and homozygous rats.
839 TUNEL staining was performed under the standard medium with or without 0.3 mM H₂O₂.
840 (F) Mitochondria and nucleus of primary neurons derived from WT and homozygous rats
841 treated with standard medium with or without 0.3 mM H₂O₂.

842
843 **Fig. 7.** *Txn1*-F54L rat generated by genome editing replicates the vacuolar degeneration in the
844 midbrain. The yellow arrowheads indicate vacuolar degeneration.

845 (A) Representative HE staining of the sagittal brain section at three weeks for each genotype.
846 (B) The coronal slices of the brain for each 500 mm section in the heterozygote.

847

848 **Supplementary Fig. 1.** Representative MRI for WT at five weeks.

849 (A) Sagittal slices.
850 (B) Coronal slices.
851 (C) Horizontal slices.

852

853 **Supplementary Fig. 2.** Representative MRI for heterozygote at five weeks.

854 (A) Sagittal slices.
855 (B) Coronal slices.
856 (C) Horizontal slices.

857

858 **Supplementary Fig. 3.** Representative MRI for homozygote at five weeks.

859 (A) Sagittal slices.

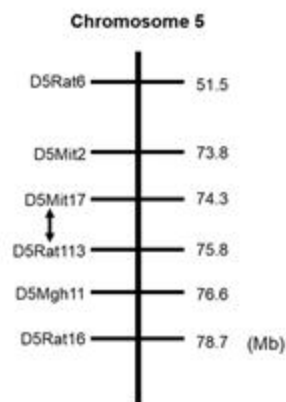
860 (B) Horizontal slices.

861

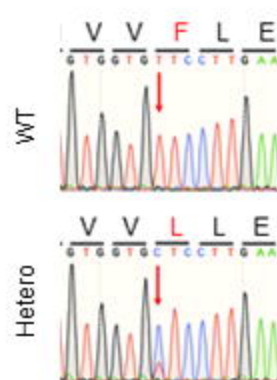
862 **Supplementary Fig. 4.** *Txn1*-F54L rat generated by genome editing replicates the transient

863 vacuolar degeneration in the midbrain from two to nine weeks of age.

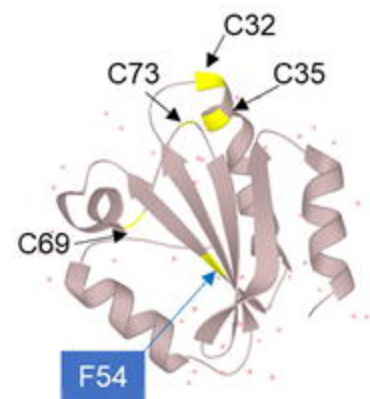
A



B

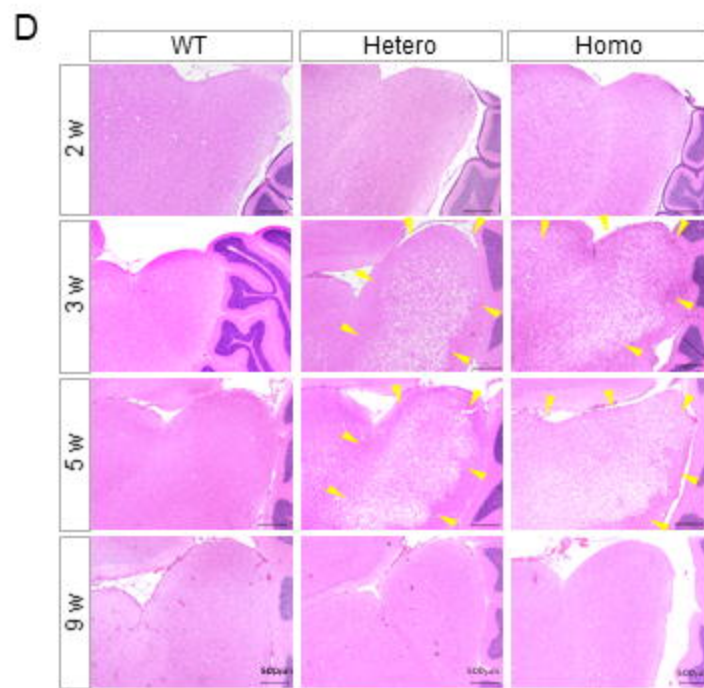
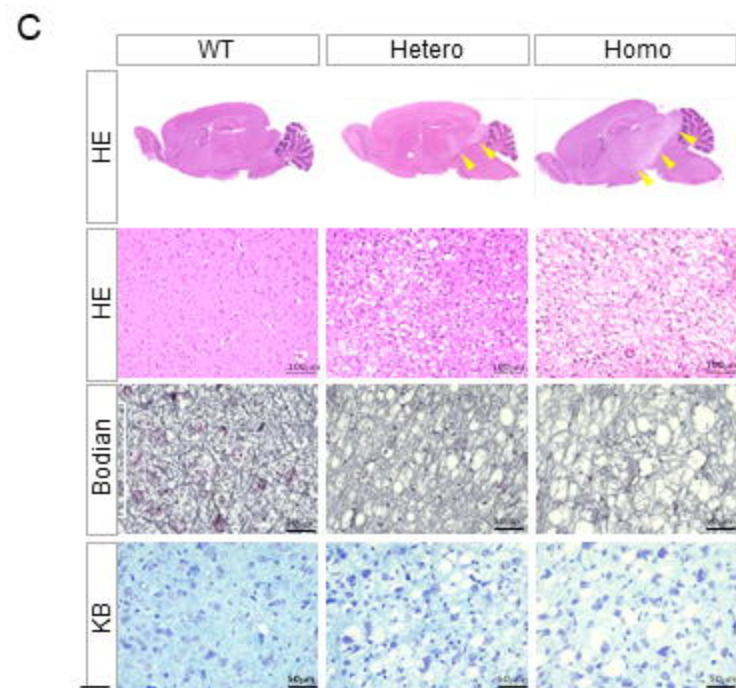
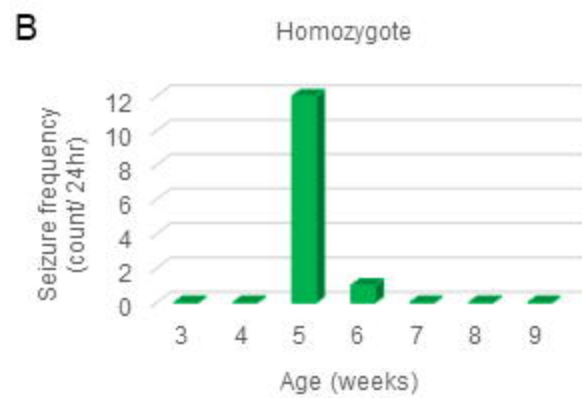
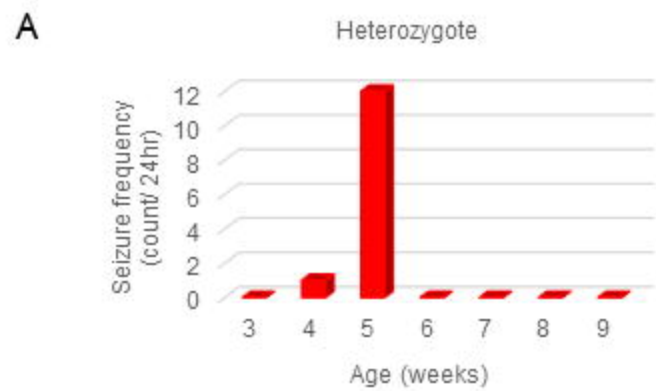


C

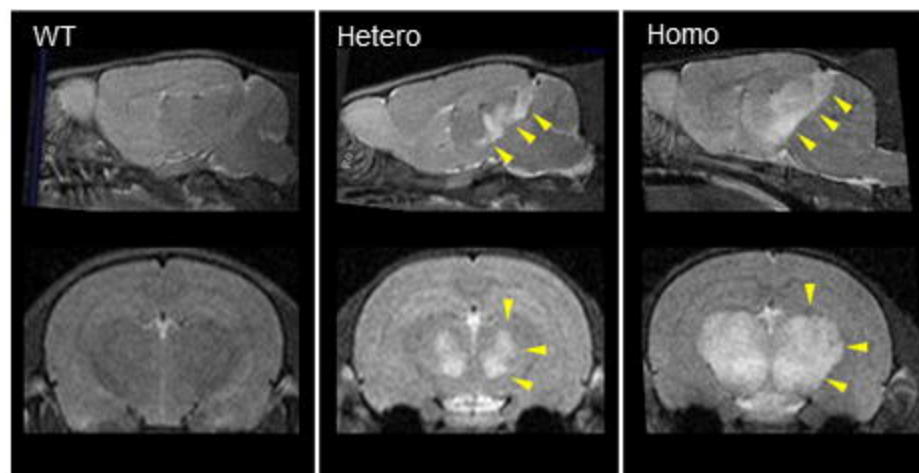


D

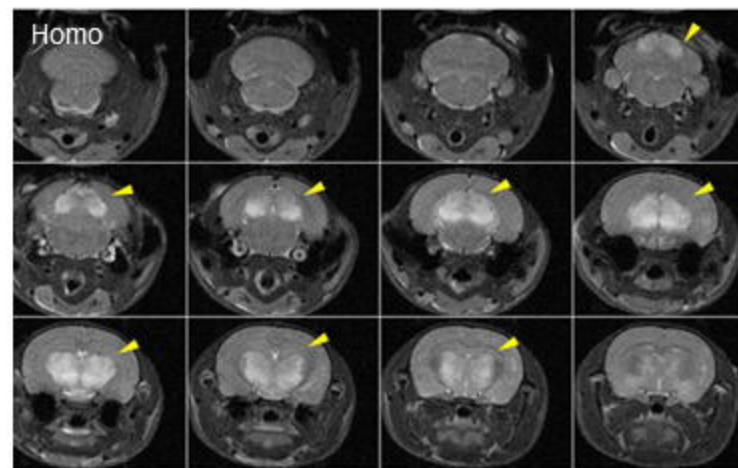
	1	32	35	54	69	73	105	
Human	MVKQIESKTAFQEALDAAGDKLVVDFSATW	CGPC	KMIKPFHSLSEKYSNVV	IFLEVDVDDCQDVASE	CEVCKMPTFQFFKKGQKVGEFSGANKEKLEATINELV			
Rat	MVKLIESKEAFQEALAAAGDKLVVDFSATW	CGPC	KMIKPFHSLCDKYSNVV	IFLEVDVDDCQDVAAD	CEVCKMPTFQFFYKKGQKVGEFSGANKEKLEASITEFA			
Mouse	MVKLIESKEAFQEALAAAGDKLVVDFSATW	CGPC	KMIKPFHSLCDKYSNVV	IFLEVDVDDCQDVAAD	CEVCKMPTFQFFYKKGQKVGEFSGANKEKLEASITEYA			
Marmoset	MVKQIDSKDAFQEALDAAGDKLVVDFSATW	CGPC	KMIKPFHSLSEKYSNVV	IFLEVDVDDCQDVASE	CEVCKMPTFQFFKKGQKVGEFSGANKEKLEATINEFV			
Sheep	MVKQIESKYAFQEALNSAGEKLVVDFSATW	CGPC	KMIKPFHSLSEKYSNVV	IFLEVDVDDCQDVAAE	CEVCKMPTFQFFKKGQKVSEFSGANKEKLEATINELI			
Horse	MVKQIESKSAFQEALNSAGEKLVVDFSATW	CGPC	KMIKPFHSLSEKYSNVV	IFLEVDVDDCQDVAAE	CEVCKMPTFQFFKKGQKVDFEFGANKEKLEATIKGLI			
Cattle	MVKQIESKYAFQEALNSAGEKLVVDFSATW	CGPC	KMIKPFHSLSEKYSNVV	IFLEVDVDDCQDVAAE	CEVCKMPTFQFFKKGQKVGEFSGANKEKLEATINELI			
Pig	MVKQIESKYAFQEALNSAGEKLVVDFSATW	CGPC	KMIKPFHSLSEKYSNVV	IFLEVDVDDCQDVASE	CEVCKMPTFQFFKKGQKVGEFSGANKEKLEATINELI			
Alpaca	MVKQIESKYAFQEALNSAGDKLVVDFSATW	CGPC	KMIKPFHSLSEKYSNVV	IFLEVDVDDCQDVASE	CEVCKMPTFQFFKKGQKVGEFSGANKEKLEATINELI			
Ferret	MVKQIESKIAFQEALVGAGDKLVVDFSATW	CGPC	KMIKPFHSLSEKYSNVV	IFLEVDVDDCQDVASE	CEVCKMPTFQFFKKGQKVGEFSGANKEKLEATINELI			
Bat	MVKQIDSKDAFEEALTSAGSKLVVDFSATW	CGPC	KMIKPFHSLSEKYSNVV	IFLEVDVDDCQDVASE	CEVCKMPTFQFFKNGKQKVGEFSGANKEKLESTINEFI			
Marmot	MVKQIESKEAFQEALNSAGDKLVVDFSATW	CGPC	KMIKPFHSLSEKYSNVV	IFLEVDVDDCQDVAAE	CEVCKMPTFQFFKKGQKVGEFSGANKEKLEATINEFV			
Guinea pig	MVQQIESKEAFQEALNDAGDKLVVDFSATW	CGPC	KMIKPFHSLSEKYSNVV	IFLEVDVDDCQDVAAE	CEVCKMPTFQFFKKGQKVSEFSGANKEKLEATINELV			
Chinchilla	MVQQIETKEAFQQAALAAAGDKLVVDFSATW	CGPC	KMIKPFHSLSEKYSNVV	IFLEVDVDDCQDVAAE	CEVCKMPTFQFFKKGQKVSEFSGANKEKLEATINELI			
Secondary structure	β	α	β	β	α	β	β	α
	β strand	α helix						



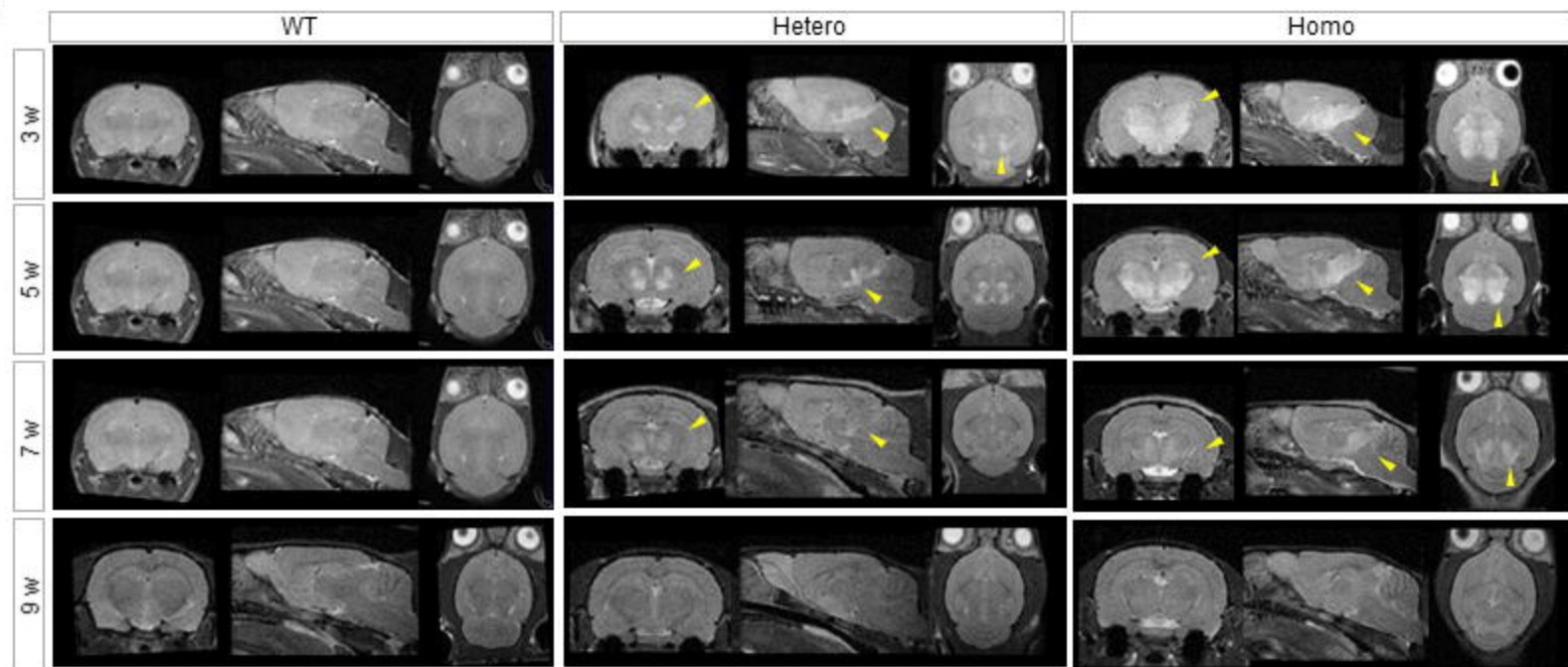
A

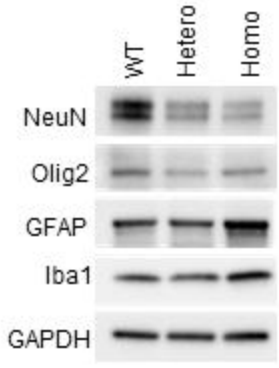
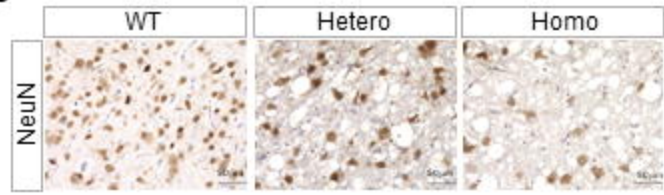
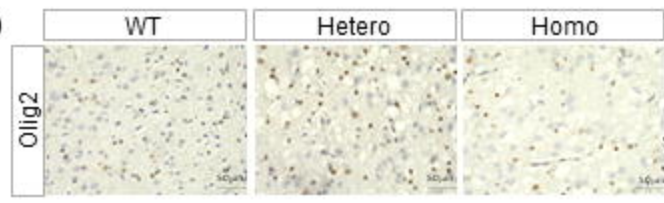
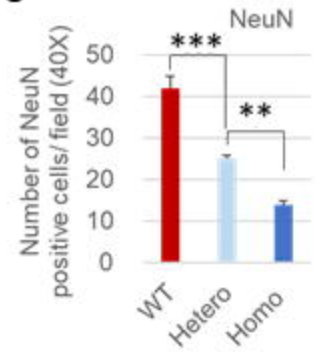


B



C



A**B****D****C****E**